The Astrophysical Journal, 676:1050–1063, 2008 April 1

ISOLATED X-RAY–INFRARED SOURCES IN THE REGION OF INTERACTION OF THE SUPERNOVA REMNANT IC 443 WITH A MOLECULAR CLOUD

A. M. Bykov,[1] A. M. Krassilchtchikov,[1] Yu. A. Uvarov,[1] H. Bloemen,[2] F. Bocchino,[3] G. M. Dubner,[4] E. B. Giacani,[4] and G. G. Pavlov[5]

Received 2007 May 11; accepted 2008 January 1

ABSTRACT

The nature of the extended hard X-ray source XMMU J061804.3+222732 and its surroundings is investigated using *XMM-Newton*, *Chandra*, and *Spitzer* observations. This source is located in an interaction region of the IC 443 supernova remnant with a neighboring molecular cloud. The X-ray emission consists of a number of bright clumps embedded in an extended structured nonthermal X-ray nebula larger than 30″ in size. Some clumps show evidence for line emission at ∼1.9 and ∼3.7 keV at the 99% confidence level. Large-scale diffuse radio emission of IC 443 passes over the source region, with an enhancement near the source. An IR source of about 14″ × 7″ size is prominent in the 24, 70, and 2.2 μm bands, adjacent to a putative Si K-shell X-ray line emission region. The observed IR/X-ray morphology and spectra are consistent with those expected for J/C-type shocks of different velocities driven by fragmented supernova ejecta colliding with the dense medium of a molecular cloud. The IR emission of the source detected by *Spitzer* can be attributed to both continuum emission from an H II region created by the ejecta fragment and line emission excited by shocks. This source region in IC 443 may be an example of a rather numerous population of hard X-ray/IR sources created by supernova explosions in the dense environment of star-forming regions. Alternative Galactic and extragalactic interpretations of the observed source are also discussed.

Subject headings: ISM: individual (IC 443) — supernova remnants — X-rays: ISM

1. INTRODUCTION

The energy release and the ejection of nucleosynthesis products by supernovae (SNe) events are of great importance for our understanding of the physics of the interstellar medium (ISM). The mixing of the ejected metals with the surrounding matter is of special interest when a SN occurs in a molecular cloud, which may cause further star-forming activity.

Optical and UV studies of the structure of SN remnants (SNRs) have revealed a complex metal composition of ejecta and the presence of isolated high-velocity ejecta fragments interacting with surrounding media. The most prominent manifestations of this phenomena are the fast-moving knots observed in some young "oxygen-rich" SNRs, such as the Galactic SNRs Cas A (e.g., Chevalier & Kirshner 1979; Fesen et al. 2006), Puppis A (Winkler & Kirshner 1985), G292.0+1.8 (e.g., Winkler & Long 2006), and also N132D in the LMC and 1E 0102.2−7219 in the SMC (e.g., Blair et al. 2000).

Ballistically, moving ejecta fragments of SNRs can be considered as a class of hard X-ray sources. The prototype was observed in the Vela SNR (Aschenbach et al. 1995; Miyata et al. 2001). A massive individual fragment moving supersonically through a molecular cloud can have a luminosity $L_S \gtrsim 10^{31}$ ergs s^{-1} in the 1–10 keV band, and is observable with *XMM-Newton* and *Chandra* at a few kpc distance (Bykov 2002, 2003). Its X-ray emission is expected to consist of two components. The first one is thermal X-ray emission from the hot shocked ambient gas behind the fragment bow shock, with a spectrum of an optically thin thermal plasma of an ISM-cloud abundance. The second emission component is nonthermal; the interaction of fast electrons accelerated at the fragment bow shock with the fragment body produces a hard continuum as well as line emission (X-ray and IR), including the K-shell lines of Si, S, Ar, Ca, Fe, and other elements ejected by SNe. Detection of the X-ray line emission would help distinguish an ejecta fragment from the other possible source of hard continuum emission associated with a SNR, namely, a pulsar wind nebula (PWN).

A young SNR of an age of a few thousands years interacting with a molecular cloud can produce hundreds of X-ray sources associated with isolated ejecta fragments. They should be particularly numerous in star-forming regions like those in the Galactic center region, where young core-collapsed supernovae in or near molecular clouds are expected to be present in abundance. The expected observational appearance of isolated ejecta fragments in a molecular cloud differs from what is seen in the Vela SNR. Ejecta fragments interacting with a dense molecular cloud are slowed down and crushed, and they are generally more bright. We will argue here that the X-ray emission spectra of ejecta fragments in a molecular cloud may be dominated by hard nonthermal components, because a powerful but very soft thermal component could be heavily absorbed. On the other hand, the spectra of fast supernova ejecta fragments propagating in a tenuous plasma, as is the case in the Vela SNR, would be long-lived, less luminous, and dominated by thermal emission.

The present paper focuses on IC 443. This is a SNR of a medium age, estimated by Chevalier (1999) to be ∼30,000 yr, for which the number of X-ray sources from ejecta fragments should be *much smaller* than in a young SNR (possibly, only a few). It is, however, the best and most reliable laboratory to study this phenomenon since there are only very few examples of clearly established SNR-cloud interactions.

[1] A. F. Ioffe Institute for Physics and Technology, St. Petersburg, Russia, 194021; byk@astro.ioffe.ru.
[2] SRON Netherlands Institute for Space Research, Sorbonnelaan 2, 3584 CA Utrecht, Netherlands.
[3] INAF–Osservatorio Astronomico "G. S.Vaiana," Piazza del Parlamento 1, 90134 Palermo, Italy.
[4] Instituto de Astronomía y Física del Espacio (IAFE), CC 67, Suc. 28, 1428 Buenos Aires, Argentina.
[5] Pennsylvania State University, 525 Davey Laboratory, University Park, PA 16802.

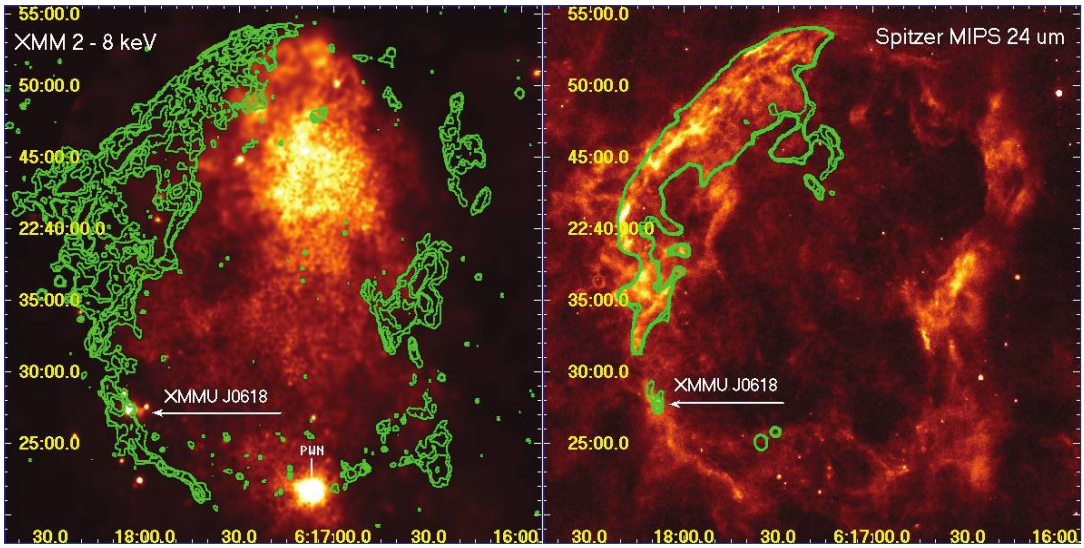

FIG. 1.—Wide-field views of SNR IC 443. *Left*: *XMM-Newton* 2–8 keV image with *Spitzer* MIPS 24 μm contours overlaid. *Right*: *Spitzer* MIPS image at 24 μm with *VLA* 1.4 GHz contours overlaid. The images are produced from the *XMM-Newton* observations 0114100101–0114100601 and 0301960101, and *Spitzer* MIPS observations r4616960, r4617216, and r4617472. The white arrow points to the studied region.

IC 443 (G189.1+3.0) is an evolved SNR of about 45′ size at a distance of 1.5 kpc (e.g., Fesen & Kirshner 1980). Radio observations of IC 443 (e.g., Braun & Strom 1986; Green 1986; Leahy 2004) show two half-shells. This appearance is probably due to interaction of the SNR with a molecular cloud that seems to separate the two half-shells. The molecular-cloud material has a torus-like structure (Cornett et al. 1977; Burton et al. 1988; Troja et al. 2006) that can be interpreted as a sheetlike cloud first broken by the expanding presupernova wind and then by the SNR blast wave. Plenty of evidence for shock-excited molecules in this region has been found (e.g., DeNoyer 1979; Burton et al. 1988; Dickman et al. 1992; Turner et al. 1992; van Dishoeck et al. 1993; Tauber et al. 1994; Richter et al. 1995; Cesarsky et al. 1999; Snell et al. 2005). The complex structure of the interaction region, with evidence for multiple dense clumps, is seen in 2MASS images (e.g., Rho et al. 2001). Three OH (1720 MHz) masers were found in IC 443 (Claussen et al. 1997; Hewitt et al. 2006 and references therein).

Soft X-ray maps of IC 443 based on *ROSAT* data (Asaoka & Aschenbach 1994) and recent radio observations (Leahy 2004) suggest that another SNR, G189.6+3.3, is seen in the IC 443 field (see also the *XMM-Newton* study by Troja et al. 2006). This makes the multiwavelength observational picture even more complex to interpret.

The field of IC 443 was observed in X-rays with *HEAO 1* (Petre et al. 1988), *Ginga* (Wang et al. 1992), *ROSAT* (Asaoka & Aschenbach 1994), *ASCA* (Keohane et al. 1997; Kawasaki et al. 2002), *BeppoSAX* (Preite-Martinez et al. 2000; Bocchino & Bykov 2000), *Chandra* (Olbert et al. 2001; Bykov et al. 2005; Gaensler et al. 2006; Weisskopf et al. 2007), *XMM-Newton* (Bocchino & Bykov 2001, 2003; Troja et al. 2006), and *RXTE* (Sturner et al. 2004).

The X-ray emission of IC 443 below 4 keV is dominated by a number of thermal components (e.g., Petre et al. 1988; Asaoka & Aschenbach 1994; Kawasaki et al. 2002; Troja et al. 2006). The thermal-emission morphology is center-filled, with soft emission filaments visible at energies below 0.5 keV. A gradient of X-ray surface brightness at the SNR limb was found, as well as strong variations of absorbing column density $N_{\rm H}$, which indicates the complex molecular-cloud environment of IC 443 in the southern part of the remnant (e.g., Asaoka & Aschenbach 1994).

ASCA observations have established that the hard X-ray emission of IC 443 (above 4 keV) is dominated by localized sources in the southern part of the remnant (Keohane et al. 1997). In *XMM-Newton* observations Bocchino & Bykov (2003, hereafter BB03) found 12 sources with fluxes over 10^{-14} ergs cm^{-2} s^{-1} in the 2–10 keV band. Six of the detected sources are located in a relatively small, of $15' \times 15'$ size, region projected onto the molecular cloud in the southeastern part of IC 443. *BeppoSAX* MECS observations (4–10 keV) showed two sources, 1SAX J0617.1+2221 and 1SAX J0618.0+2227, with evidence from the *BeppoSAX* PDS for the presence of hard emission up to 100 keV for the former (Bocchino & Bykov 2000). Observations of this source by *Chandra* (Olbert et al. 2001; Gaensler et al. 2006; Weisskopf et al. 2007) and *XMM-Newton* (Bocchino & Bykov 2001) established its plerionic nature. Leahy (2004) argued that the pulsar that powers this plerion is associated with G189.6+3.3 rather than IC 443. The nature of the second hard source—1SAX J0618.0+2227—remained unknown. This source, the brightest in the region (excluding the plerion), was resolved with *XMM-Newton* into two sources—the extended XMMU J061804.3+222732 (of $\sim$20″ sized) and the pointlike XMMU J061806.4+222832. We will call them sources 1 and 2, respectively (note that the sources were listed as Src 11 and Src 12 in BB03). The position of XMMU J061804.3+222732 in the remnant is illustrated in Figures 1 and 2.

A dedicated *Chandra* observation of source 1 has revealed a complex structure of a few bright clumps embedded in extended emission of >20″size (Bykov et al. 2005, hereafter BBP05). The brightest clumps are the extended source 1a and the pointlike source 1b. The apparent position of the source in a SNR–molecular cloud interaction region naturally leads to SNR-related interpretations. The observed X-ray morphology of source 1 and the spectra of its components are consistent with expectations for a SN ejecta fragment interacting with a dense ambient medium. Alternatively, source 1 could be interpreted as a PWN associated with either IC 443 or G189.6+3.3 (BBP05). However, one cannot exclude the extragalactic origin of the source, that is discussed in some detail in § 4.7.

IC 443 is a candidate counterpart of the EGRET γ-ray source 3EG J0617+2238, with a flux of about 5×10^{-7} cm^{-2} s^{-1} above 100 MeV (Esposito et al. 1996). The spectrum of source 1

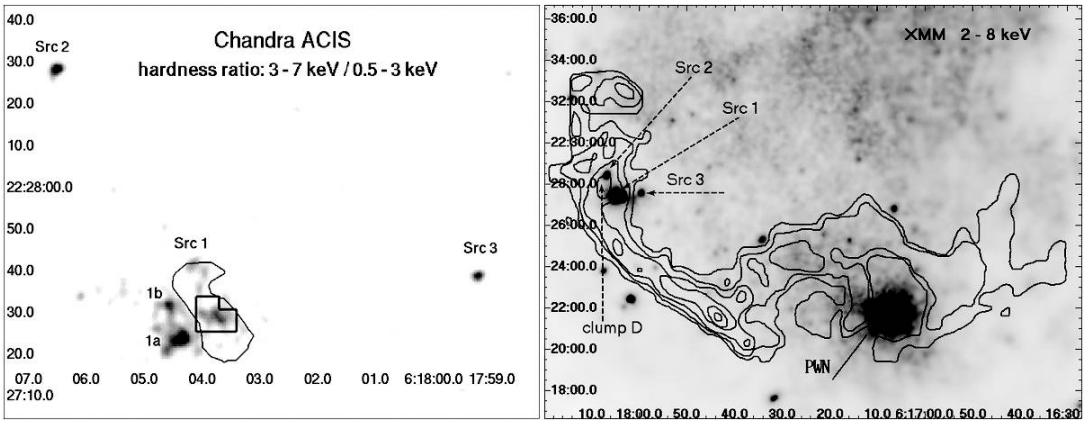

FIG. 2.—X-ray images of the region under consideration. The data are from the *Chandra* observation 4675 and from *XMM-Newton* observations 0114100101–0114100601 and 0301960101. *Left*: *Chandra* hardness ratio image (a 3.0–7.0 keV countrate map divided by a 0.5–3.0 keV countrate map) together with a contour outlining the extended near-IR source 2MASS J06180378+2227314 (with the L-shaped Si K-shell X-ray emission-line region inside). Broadband *Chandra* maps of the region have been presented by BPP05. *Right*: *XMM-Newton* image in the 2–8 keV band with superimposed contours of 2.122 μm H_2 emission of Burton (1987, adopted from van Dishoeck et al. 1993), indicating the presence of a shocked molecular cloud. The studied X-ray sources are indicated as well as the clump D of van Dishoeck et al. (1993).

extrapolated into the EGRET range is consistent with that of 3EG J0617+2238 (BBP05). Also, the position of source 1 is consistent (albeit marginally) with that of 3EG J0617+2238. Such a γ-ray luminosity can be expected for both the fragment and PWN interpretations. The forthcoming *GLAST* mission (e.g., Johnson 2006) will be able to provide an accurate position and spectrum of 3EG J0617+2238, thus helping to solve the issue. Source 1 lies far away from the 99% error circle of the TeV-regime source recently reported by MAGIC (Albert et al. 2007) in the western part of IC 443 field. The apparent position of TeV MAGIC source is close to the 1720 MHz OH maser detected by Claussen et al. (1997).

We present here new results of a deep 80 ks observation of the region with *XMM-Newton*, imaging of the region with the *Spitzer* infrared observatory, and a new analysis of VLA radio observations. In § 2 a combined analysis of the new *XMM-Newton* observations and all the previous high-resolution X-ray data from *Chandra* and *XMM-Newton* is presented, including images, spectra, and time variations in the X-ray domain. In § 3 archival radio (VLA), IR (2MASS and *Spitzer* MIPS), and optical (POSS-II) data are used to constrain the nature of source 1. A discussion of the obtained results and future prospects are presented in § 4.

2. X-RAY DATA ANALYSIS

XMMU J061804.3+222732 (source 1) was observed with *XMM-Newton* in 2000 and 2006, and with *Chandra* in 2000 and 2004 (Table 1). CIAO version 3.0 with CALDB version 3.2.2 was used for *Chandra* data processing, SAS version 20060628_1801-7.0.0 for *XMM-Newton* data processing, and the HEASOFT 6.1 suite, including XSPEC version 12.3, for spectral fitting.

In the course of *XMM-Newton* data reduction, patterns 0–4 of EPIC-pn detector events and patterns 0–12 of MOS events were used. To filter out the periods of enhanced particle background, we applied a standard method of soft flare detection.[6] The filtering did not significantly change the good time for the data taken in 2000, but reduced it in the data set of 2006.

In the *Chandra* observation of the year 2000, source 1 is offset 17.6′ from the ACIS aim point, on chip S4. To increase the quality of the ACIS chip S4 data the standard procedure was used to create an event2 file from the archival event1 file, including a run of the `destreak` task. As a result, the good time of the observation decreased from 11.5 to 9.6 ks. An appropriate webscript[7] was used to correct the *Chandra* event files for the systematic position offset.

Figure 1 shows a wide-field view of IC 443, both in X-rays and in the medium IR 24 μm band. Two X-ray images of the source region of interest here, obtained with *Chandra* and *XMM-Newton*, are presented in Figure 2. The coordinates of source 1a and source 1b obtained from the *Chandra* data with the `celldetect` algorithm ($\alpha = 06^{h}18^{m}04.32^{s}$, $\delta + 22^{\circ}27'24.1''$, and $\alpha = 06^{h}18^{m}04.58^{s}$, $\delta = +22^{\circ}27'31.8''$, respectively) do not differ from those reported by BBP05, as well as the position of

[6] See http://heasarc.gsfc.nasa.gov/docs/xmm/abc/node7.html.
[7] See http://asc.harvard.edu/cal/ASPECT/fix_offset/fix_offset.cgi.

TABLE 1
X-RAY OBSERVATIONS OF XMMU J061804.3+222732

ObsID	Observatory	Instrument	Date of Observation	Exposure (ks)	Good Time (ks)
760.....	*Chandra*	ACIS-S	2000 Apr 10/11	11.5	9.6
		pn		23.2	19.5
0114100301.....	*XMM-Newton*	MOS1	2000 Sep 27	25.6	25.1
		MOS2		25.6	25.1
4675.....	*Chandra*	ACIS-S	2004 Apr 12/13	58.4	56.2
		pn		79.9	52.9
0301960101.....	*XMM-Newton*	MOS1	2006 Mar 30/31	81.6	67.6
		MOS2		81.6	68.2

TABLE 2
PARAMETERS OF ABSORBED POWER-LAW MODELS OF SOURCES 1, 2, AND 3

Source (Radius)/Background	Observatory, Year	Source Counts	N_H[a]	Γ	Normalization[b]	χ^2_ν/dof
Source 1 (20″)/bkg2	*XMM-Newton* 2000 A	1064/505/507	$0.5^{+0.3}_{-0.2}$	$1.2^{+0.3}_{-0.2}$	$2.8^{+1.4}_{-0.9}10^{-5}$	1.13/124
	XMM-Newton 2006 A	4574/1899/2150	$0.5^{+0.1}_{-0.1}$	$1.3^{+0.1}_{-0.04}$	$3.2^{+0.6}_{-0.5}10^{-5}$	1.05/418
	Chandra 2004	2973	$0.7^{+0.2}_{-0.1}$	$1.5^{+0.2}_{-0.2}$	$6.7^{+2.2}_{-1.4}10^{-5}$	0.84/151
Source 1 (10″)/bkg1	*Chandra* 2004	1314	$0.2^{+0.1}_{-0.1}$	$1.0^{+0.2}_{-0.2}$	$1.4^{+0.4}_{-0.3}10^{-5}$	0.97/73
Source 2 (20″)/bkg2	*XMM-Newton* 2000 A	955/418/470	$0.8^{+0.2}_{-0.2}$	$2.3^{+0.3}_{-0.1}$	$9.4^{+3.9}_{-2.5}10^{-5}$	0.94/107
	XMM-Newton 2006 B	–/944/1003	$1.0^{+0.5}_{-0.3}$	$2.7^{+0.5}_{-0.3}$	$5.2^{+4.6}_{-2.0}10^{-5}$	0.88/105
	Chandra 2004	1829	$1.2^{+0.3}_{-0.2}$	$2.6^{+0.3}_{-0.3}$	$12.2^{+7.2}_{-3.8}10^{-5}$	0.98/94
Source 2 (10″)/bkg1	*Chandra* 2004	1270	$0.9^{+0.2}_{-0.2}$	$2.4^{+0.2}_{-0.2}$	$9.3^{+3.7}_{-2.3}10^{-5}$	1.05/66
Source 3 (20″)/bkg2	*XMM-Newton* 2000 B	–/235/225	$0.5^{+3.0}_{-0.5}$	$2.1^{+2.8}_{-1.5}$	$1.0^{+19}_{-1.0}10^{-5}$	1.15/26
	XMM-Newton 2006 A	2730/940/1080	$0.6^{+0.6}_{-0.4}$	$1.6^{+0.4}_{-0.3}$	$1.1^{+0.9}_{-0.4}10^{-5}$	1.10/234
	Chandra 2004	1251	$0.3^{+0.5}_{-0.3}$	$1.5^{+0.6}_{-0.6}$	$1.0^{+1.2}_{-1.0}10^{-5}$	1.10/66
Source 3 (10″)/bkg1	*Chandra* 2004	620	$0.7^{+0.4}_{-0.2}$	$1.9^{+0.4}_{-0.3}$	$1.7^{+1.3}_{-0.7}10^{-5}$	1.36/34

NOTES.—"A" means pn , MOS1, MOS2 data combined, while "B" means MOS1 and MOS2 data combined; "bkg1" denotes a background annulus with inner radius of 10″and outer radius of 20″, and bkg2" denotes a background annulus with inner radius of 20″and outer radius of 30″. The source counts in the third column are given as pn/MOS1/MOS2 for *XMM-Newton* and ACIS for *Chandra*. All errors quoted in the table are at the 90% confidence level for one interesting parameter.

[a] N_H is in units of 10^{22} cm^{-2}.

[b] Normalization parameter is the spectral flux in photons cm^{-2} s^{-1} keV^{-1} at 1 keV.

source 2 ($\alpha = 06^h18^m06.53^s$, $\delta = +22°28'28.2''$). A nearby source, which we refer to as source 3, is located at $\alpha = 06^h17^m59.25^s$, $\delta = +22°27'38.9''$. In addition, the *XMM-Newton* data show evidence for an extended "bridge" of diffuse emission between source 1 and source 3 (see Figs. 1, 2, and 6). On the timescale of about 6 yr, covered by the *XMM-Newton* observations used here (Table 1), it is not possible to detect a proper motion of the sources at a 1.5 kpc distance if they move with a transverse velocity $\lesssim$3000 km s^{-1}.

2.1. *Source Spectra*

The line of sight to the source region intersects the supernova shell(s), the interior of the remnant, and the molecular cloud, each having different physical parameters. Therefore, the X-ray emission detected along the line of sight has multiple thermal and nonthermal components, in addition to the Galactic background. A SNR shell can be characterized by a power-law emission spectrum, the hot low-density interiors — by thermal plasma emission, and a dense molecular cloud may cause an appreciable absorption.

We have performed a series of spectral studies of sources 1, 2, and 3, the results being presented in Table 2 (power-law models), Table 3 (thermal models), and in the text of this subsection. MEKAL thermal plasma models were used (e.g., Kaastra 1992) and the `wabs` model for absorption was applied (Morrison & McCammon 1983). Because of strong gradients in the soft X-ray surface brightness, one should carefully choose regions for spectral analysis. For the *Chandra* analysis, circular source regions of 10″radius surrounded by 10″ wide background annuli were used. For *XMM-Newton*, whose point-spread function (PSF) is broader, source regions of 20″radius and annuli with 10″width were used. That results in an underestimation of a source flux caused by subtraction of the source photons regarded as background photons due to the wide *XMM-Newton* PSF wings. The effect is estimated to be about 20% of the source flux. That may account for the differences in the *Chandra* and *XMM-Newton* normalizations

TABLE 3
PARAMETERS OF ABSORBED PLASMA (MEKAL) MODELS OF SOURCES 1, 2, AND 3

Source (Radius)/Background	Observatory, Year	Source Counts	N_H[a]	T, keV	Normalization[b]	χ^2_ν/dof
Source 1 (20″)/bkg2	*XMM-Newton* 2000 A	1064/505/507	$0.5^{+0.2}_{-0.1}$	$79.9^{+0}_{-59.6}$	$1.9^{+0.2}_{-0.4}10^{-4}$	1.1/124
	XMM-Newton 2006 A	4574/1899/2150	$0.4^{+0.1}_{-0.1}$	$75.1^{+4.8}_{-37.6}$	$1.8^{+0.1}_{-0.2}10^{-4}$	1.1/418
	Chandra 2004	2973	$0.6^{+0.1}_{-0.1}$	$24.6^{+55.3}_{-10.8}$	$2.7^{+0.5}_{-0.2}10^{-4}$	0.85/151
Source 1 (10″)/bkg1	*Chandra* 2004	1314	$0.3^{+0.1}_{-0.1}$	$79.8^{+0.1}_{-50.4}$	$1.1^{+0.1}_{-0.2}10^{-4}$	0.93/73
Source 1* (20″)/bkg2	*Chandra* 2004	1781	$1.1^{+0.5}_{-0.4}$	$5.3^{+11.4}_{-2.4}$	$1.2^{+0.5}_{-0.3}10^{-4}$	0.93/78
Source 2 (20″)/bkg2	*XMM-Newton* 2000 A	955/418/470	$0.7^{+0.3}_{-0.2}$	$3.5^{+1.3}_{-0.8}$	$1.9^{+0.5}_{-0.3}10^{-4}$	1.1/107
	XMM-Newton 2006 B	–/944/1003	$1.0^{+0.4}_{-0.4}$	$2.2^{+1.2}_{-0.6}$	$8.6^{+3.1}_{-2.6}10^{-5}$	0.98/105
	Chandra 2004	1829	$0.9^{+0.3}_{-0.2}$	$3.1^{+1.1}_{-0.7}$	$1.8^{+0.4}_{-0.3}10^{-4}$	1.2/94
Source 2 (10″)/bkg1	*Chandra* 2004	1270	$0.7^{+0.2}_{-0.2}$	$3.7^{+1.3}_{-0.8}$	$1.5^{+0.3}_{-0.2}10^{-4}$	1.4/66
Source 3 (20″)/bkg2	*XMM-Newton* 2000 B	–/235/225	$0.3^{+2.6}_{-0.3}$	$7.2^{+72.7}_{-6.0}$	$1.9^{+5.4}_{-1.9}10^{-5}$	1.2/26
	XMM-Newton 2006 A	2730/940/1080	$0.4^{+0.3}_{-0.2}$	$36.7^{+42.2}_{-22.8}$	$4.0^{+1.0}_{-0.6}10^{-5}$	1.2/234
	Chandra 2004	1251	$0.4^{+0.4}_{-0.3}$	$8.1^{+71.8}_{-4.1}$	$3.9^{+1.2}_{-0.9}10^{-5}$	1.1/66
Source 3 (10″)/bkg1	*Chandra* 2004	620	$0.6^{+0.3}_{-0.2}$	$4.3^{+3.7}_{-1.4}$	$4.8^{+1.2}_{-0.9}10^{-5}$	1.3/34

NOTES.— "A" means pn, MOS1, MOS2 data combined, while "B" means MOS1 and MOS2 data combined; "bkg1" denotes a background annulus with inner radius of 10″and outer radius of 20″, and "bkg2" denotes a background annulus with inner radius of 20″and outer radius of 30″. The source counts in the third column are given as pn/MOS1/MOS2 for *XMM-Newton* and ACIS for *Chandra*. All errors quoted in the table are at the 90% confidence level for one interesting parameter. Source 1* is the annulus region of source 1(20″) with the removed 11″radius circle containing sources 1a and 1b.

[a] N_H is in units of 10^{22} cm^{-2}.

[b] MEKAL model normalization parameter: $K = 10^{-14}/\left[4\pi D^2(1+z)^2\right]\int n_e n_H\, dV$, where D is the angular size distance to the source in cm, n_e and n_H are the electron and hydrogen density in cm^{-3}, and integration is done over source volume.

of the fitted source flux reported in Table 2. However, the fitted power-law indices and absorption values are not affected.

When comparing the *Chandra* and *XMM-Newton* spectra, such enlarged source extraction regions were also used for the *Chandra* data. For the spectral fitting, the count rate spectra were grouped with a minimum of 15 counts bin^{-1}. Table 2 summarizes the results of spectral fitting for source 1, source 2, and source 3 with an absorbed power law (using the `wabs` model for absorption; Morrison & McCammon 1983). Thermal plasma models for sources 1 and 3 yield very high and poorly constrained values of the temperature. However, the spectrum of source 2 can be as well described with a MEKAL model as an absorbed emission of thermal plasma (see Table 3).

The high angular resolution of *Chandra* ACIS is useful for studying the spectra of the substructure of source 1 in more detail. A $2'' \times 4''$ elliptical source region around source 1a, and a $2''$ radius source region around source 1b were selected. For both regions, the background counts were extracted from an annulus with inner radius of $10''$and outer radius of $20''$ centered between the two sources. The spectrum of source 1a can be described as an absorbed [$N_{\rm H} = (1.1 \pm 0.8) \times 10^{22}$ cm^{-2}] power law with photon index $\Gamma = 1.5^{+0.5}_{-0.4}$ and a thermal plasma component with $T = 0.2^{+0.6}_{-0.1}$ keV. The reduced χ^2 of this fit is 0.71 at 14 degrees of freedom (dof). The spectrum of source 1b can be described as an absorbed ($N_{\rm H} = 1.2^{+1.0}_{-0.9} \times 10^{22}$ cm^{-2}) power law with photon index $\Gamma = 2.0^{+0.9}_{-0.7}$. The reduced χ^2 of this fit is 0.73 at 9 dof. The quoted errors are at the 90% confidence level (for one interesting parameter). The confidence contours for the spectral parameters of the whole source 1 are shown in Figure 3. These results are in a good agreement with those obtained by BBP05.

The best-fit value of $N_{\rm H}$ for a power-law model of source 1a (that dominates the $10''$ radius source 1 in Table 2, line 4) is well below that for the southeastern region of IC 443 obtained with *ROSAT* and *XMM-Newton* (7×10^{21} cm^{-2}). If one assumes that source 1a, source 1b, and the extended hard emission are at the same column density $N_{\rm H} \sim 7 \times 10^{21}$ cm^{-2}, one has to add a soft thermal component (of $T \gtrsim 0.1$ keV) for source 1a (see Fig. 3 in BBP05). Results of such fits, with the additional optically thin thermal plasma emission (MEKAL) component for source 1a, are presented in Table 1 of BBP05. Such a component is localized in source 1a and can be explained if the source is a supersonic ejecta fragment (given a range of shock velocities up to 300 km s^{-1}).

Moreover, BBP05 showed that a satisfactory fit can be also obtained with a blackbody component used instead of MEKAL. Such a blackbody plus power-law fit, with a temperature of about 0.1 keV, radius of about 3 km, and power-law index of about 1.3 (at fixed $N_{\rm H} = 7 \times 10^{21}$ cm^{-2}) can be understood—if source 1a is a pulsar wind nebula—as a combination of thermal emission from the surface of a neutron star plus nonthermal emission from the neutron star magnetosphere and/or surrounding pulsar wind nebula.

It should be noted that the high plasma temperatures obtained to fit a thermal model to the *Chandra* spectrum of the region of a $20''$ radius around source 1 are due to a contribution of hard spectra of source 1a, source 1b, and their neighborhood. If one considers the spectrum of this circle region with a removed inner circle of $11''$radius surrounding source 1a and source 1b (the resulting annulus is named source 1^* in Table 3), one obtains a fit with $N_{\rm H} = 1.1^{+0.5}_{-0.4} \times 10^{22}$ cm^{-2}, $T = 5.3^{+11.4}_{-2.4}$ keV with $\chi^2 = 0.93$ at 78 dof.

A line feature centered at $\approx$1.8 keV is seen (Fig. 4, *top row*) at the 99% confidence level in the *XMM-Newton* spectrum extracted from the extended nebula of source 1—the L-shaped region shown in the left panel of Figure 2. The combined MOS1+pn+ACIS spectrum of the L-shaped region can be modeled as an absorbed

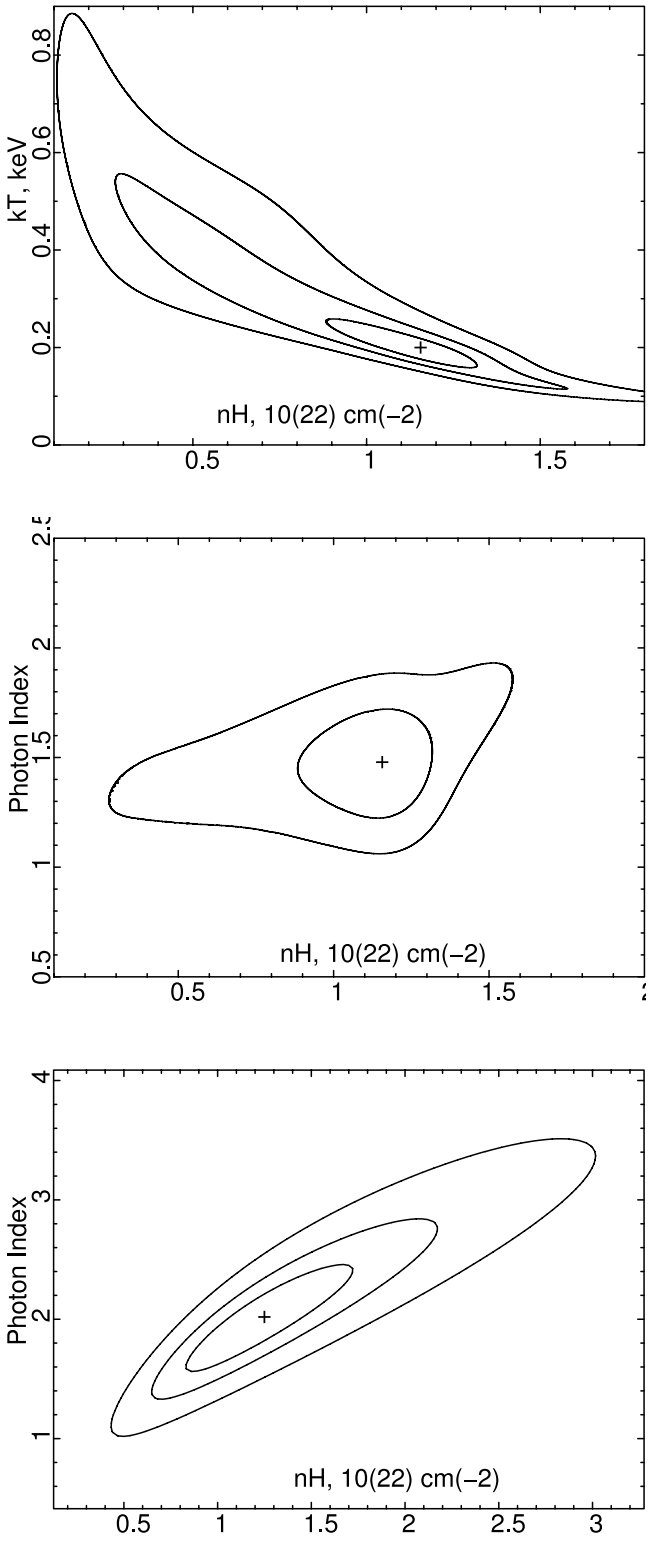

FIG. 3.—Confidence contours (68%, 90%, and 99% confidence levels) for the spectral fit parameters of source 1 spectra obtained with *Chandra*. *Top and middle panels*: Temperature and photon index vs. hydrogen column density for a two-component thermal plasma + power-law model. *Bottom panel*: Photon index vs. hydrogen column density for an absorbed power law model. The outer contour on the central panel runs outside the shown parameter space.

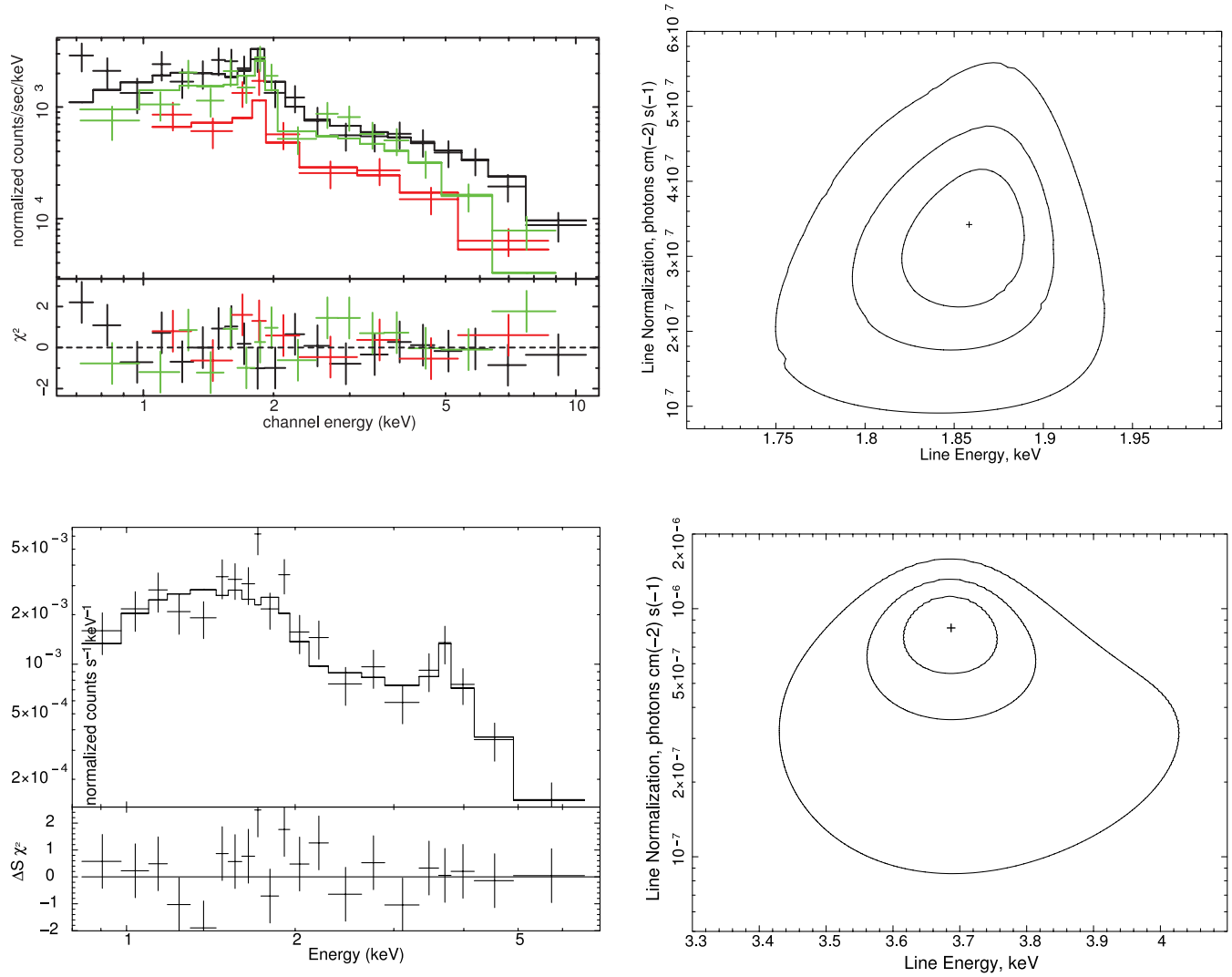

FIG. 4.—*Top Left*: X-ray spectrum of the L-shaped region (shown in Fig.2) derived from a combination of the MOS1, pn (obs. 2006), and ACIS (obs. 2004) data. The model (*histograms*) corresponds to an absorbed [$N_{\rm H} = (0.3 \pm 0.2) \times 10^{22}$ cm^{-2}] power law with $\Gamma = 1.1^{+0.3}_{-0.2}$ and a possible Si line at 1.9 ± 0.1 keV of a fixed 0.1 keV width. *Top right*: 68%, 90%, and 99% confidence contours for the parameters of the 1.8 keV Si K-shell line for the L-shaped region, shown in Fig. 2, obtained from combined data of the MOS1, pn (obs. 2006), and ACIS (obs. 2004) detectors. *Botton left*: X-ray spectrum of source 3 extracted from *Chandra* observations. The spectrum is modeled as an absorbed ($N_{\rm H} = 0.6^{+0.4}_{-0.2} \times 10^{22}$ cm^{-2}) power law with $\Gamma = 1.8^{+0.4}_{-0.3}$ and a possible Ar line at 3.7 ± 0.1 keV of a $0.2^{+0.6}_{-0.2}$ keV width. *Bottom right*: 68%, 90%, and 99% confidence contours for the parameters of the 3.7 keV Ar K-shell line for source 3. All the quoted errors are at the 90% confidence level.

$N_{\rm H} = (0.3 \pm 0.2) \times 10^{22}$ cm^{-2} power law with $\Gamma = 1.1^{+0.3}_{-0.2}$ and a possible Si line at 1.9 ± 0.1 keV of a fixed 0.1 keV width.

To investigate the *Chandra* spectrum of the pointlike source 3, source counts were extracted from a small circle of 2″ radius. The background counts were taken from an annulus with the inner radius of 3″ and the outer radius of 10″. The spectrum is shown in Figure 4 (*bottom row*). It contains a feature at 3.7 keV that is possibly due to an Ar emission line. There is, however, an alternative possible interpretation of the line as a redshifted Fe K line that assumes that source 3 is extragalactic.

The *XMM-Newton* spectrum of the faint bridge between source 1 and source 3 can be modeled either as absorbed ($N_{\rm H} = 0.5^{+0.3}_{-0.7} \times 10^{22}$ cm^{-2}) thermal plasma ($T = 5.5^{+3.7}_{-9.5}$ keV) emission with $\chi^2_\nu = 0.79$ at 74 dof or as an absorbed ($N_{\rm H} = 0.6^{+0.4}_{-0.8} \times 10^{22}$ cm^{-2}) power law of photon index $\Gamma = 2.0^{+1.8}_{-2.1}$ with $\chi^2_\nu = 0.74$ at 74 dof.

The 20″–aperture *Chandra* spectra of the studied sources, sources 1, 2, and 3, can be simultaneously modeled by an absorbed ($N_{\rm H} = 0.8^{+0.2}_{-0.1} \times 10^{22}$ cm^{-2}) power law of the photon index $\Gamma = 1.8 \pm 0.2$ with $\chi^2_\nu = 1.1$ at 315 dof or by a thermal plasma (MEKAL) model with $N_{\rm H} = (0.6 \pm 0.1) \times 10^{22}$ cm^{-2}, and $T = 12^{+7}_{-3}$ keV with $\chi^2_\nu = 1.1$ at 315 dof.

Using all the data available, we found that source 1 has not shown a significant time variation, its flux being consistent with that originally obtained by BB03. Some evidence (at the 90% confidence level) is found for time variation in the unabsorbed flux of sources 2 and 3, as illustrated in Figure 5. The unabsorbed flux of source 2 in the 0.5–10 keV band decreased between 2000 September and 2006 March with 99% confidence. In the 2–10 keV band the flux increased between 2000 April and 2000 September and later decreased with 90% confidence. The unabsorbed flux of source 3 increased between 2000 September and 2006 March with 90% confidence. More observations are needed to firmly conclude on the issue.

3. RADIO, IR, AND OPTICAL DATA ANALYSIS

3.1. *VLA Data Analysis*

A radio image of IC 443 was obtained from archival VLA[8] data obtained in 1997 at 1465 MHz from observations in the C and

[8] The VLA of the NRAO is a facility of the NSF, operated under cooperative agreement by Associated Universities, Inc.

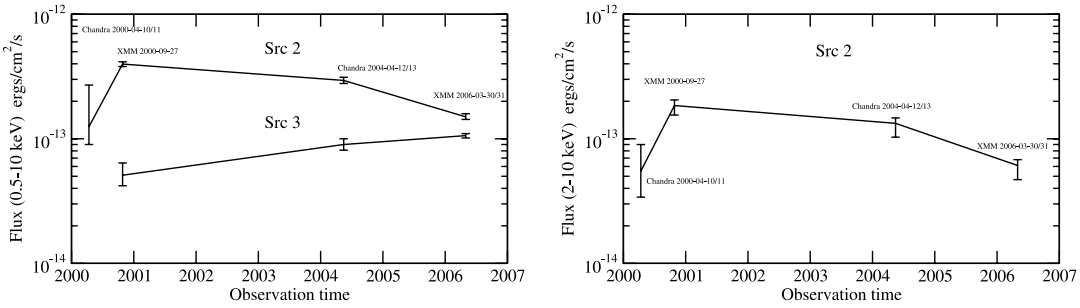

FIG. 5.—*Left*: Fluxes of sources 2 and 3 as a function of time in the 0.5–10 keV range. The errors are given at the 68% confidence level. *Right*: Fluxes of source 2 in the 2–10 keV range.

D arrays. The interferometric image has an angular resolution of $14.1'' \times 13.2''$. To recover information at all spatial frequencies, the synthesis data were combined with single dish data from the survey at 1408 MHz carried out with the 100 m MPIfR telescope (Reich et al. 1990). The final high-fidelity image has an angular resolution of $37.8'' \times 34.3''$, P.A. $= 46.5^\circ$, and an average rms noise $\sim$0.1 mJy beam^{-1}. The total integrated flux density over the whole IC 443, $S = (58 \pm 2)$ Jy, is in a good agreement with the total integrated flux obtained from single-dish observations ($S \sim 60$ Jy; Mufson et al. 1986), which assures the accuracy of flux density estimates over selected portions of the SNR.

Figure 1 (*right panel*) shows the contours of the $\lambda \sim 20$ cm emission of SNR IC 443 superimposed on a 24 μm *Spitzer* map. The radio map for the source region of interest made from interferometric data only is shown in Figure 6 as contours on a 2–8 keV *XMM-Newton* X-ray image. This figure shows that source 1 lies at the periphery of IC 443, far from the main SNR radio shell (that is situated in the northeast of the remnant), but near a localized radio excess. At the angular resolution and sensitivity of the present data, no radio continuum source, either pointlike or extended, could be associated with any of the X-ray sources. The local radio flux density, obtained by integrating the radio emission over the region containing 97% of the *XMM-Newton* counts of XMMU J061804.3+222732, is (60 ± 3) mJy.

3.2. *Spitzer MIPS Imaging and Photometry*

The field of IC 443 was the target of *Spitzer* MIPS scan observations r4616960, r4616960, and r4616960 performed on 2005 November 9 (PI: G. Rieke). The Multiband Imaging Photometer for *Spitzer* (MIPS) aboard the *Spitzer Space Telescope* (Werner et al. 2004) is capable of imaging and photometry in broad medium-IR spectral bands centered at 24, 70, and 160 μm, and low-resolution spectroscopy between 55 and 95 μm (Rieke et al. 2004). The 24 μm band covers the range of 21.3–26.1 μm, and the 70 μm band covers the range of 61.5–80.5 μm. Sources 1, 2, and 3 were outside the field of view of the *Spitzer* IRAC near-IR camera.

We used the standard MOPEX 030106 software (Makovoz et al. 2006) to construct mosaic images and extract point sources from the archival BCD-level data (preprocessed by the S13 pipeline) according to the recipes in the *Spitzer* cookbooks[9] and the MIPS data handbook.[10] The first frames of each sequence were ignored. A total of 5940 individual frames were mosaiced for each of the MIPS bands. The net exposure of the mosaic maps is equal to 65–92 frames (2.62 s each) for the 24 μm band and 12–15 frames (3.15 s each) for the 70 μm band (different parts of the map were obtained with different effective exposures). Outlier detection was performed to exclude moving and solar system objects. A wide-field *Spitzer* MIPS image of the whole remnant is shown in Figure 1.

Using the APEX software suite (Makovoz et al. 2006), we detected two pointlike sources, at $\alpha = 06^{\rm h}18^{\rm m}04.0^{\rm s}$, $\delta = +22^\circ 27' 23''$ and at $\alpha = 06^{\rm h}18^{\rm m}04.0^{\rm s}$, $\delta = +22^\circ 27' 33''$. The sources were detected only in the 24 μm band with fluxes 1.77 ± 0.07 mJy (S/N = 8.2) and 1.89 ± 0.07 mJy (S/N = 8.0), respectively. The

[9] See http://ssc.spitzer.caltech.edu/documents/datademos.
[10] See http://ssc.spitzer.caltech.edu/mips/dh.

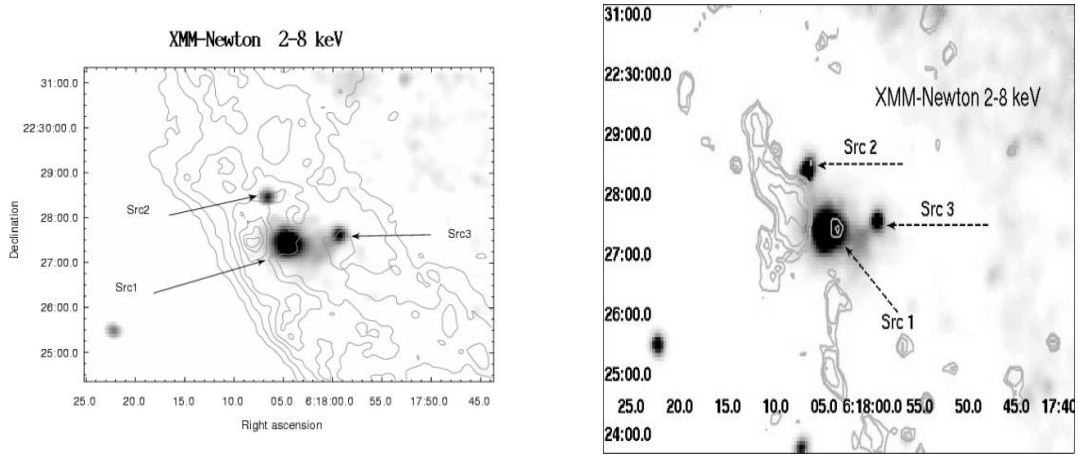

FIG. 6.—*Left*: Contours of radio surface brightness at $\lambda = 20$ cm superimposed on the *XMM-Newton* X-ray image in the 2–8 keV energy band. The angular resolution of the radio data is $14.1'' \times 13.2''$. The radio contours are plotted at 1.2, 2.4, 3.6, 4.9, 6.1, 7.3, 8.0, and 8.6 mJy beam^{-1}. *Right*: Contours of 24 μm emission detected by MIPS *Spitzer* superimposed on the *XMM-Newton* X-ray image in the 2–8 keV energy band.

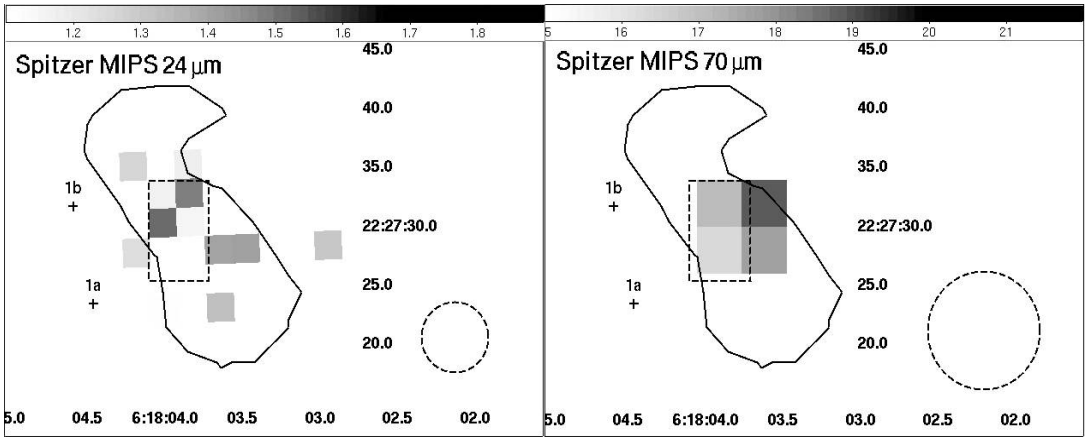

FIG. 7.—Source 1 environment as seen by *Spitzer* MIPS. The sources detected by *Chandra* are shown as crosses (3–8 keV) and a dashed rectangle (1.8–2.0 keV). The black contour denotes the extended near-IR source 2MASS J06180378+2227314. The dashed circles denote the beam size of MIPS.

latter source coincides with the absorbed near-IR source 2MASS J06180406+2227345 detected only in the K_s band ($J > 17.9$, $H > 17.0$, $K_s = 15.3 \pm 0.2$). The dereddened K_s (2.02–2.30 μm) flux of the source ranges from 0.64 to 1.21 mJy (considering the uncertainty of the extinction value), that is $(1.2–2.2) \times 10^{-13}$ ergs cm^{-2} s^{-1}.

According to the extinction maps of Schlegel et al. (1998), the total Galactic absorption toward source 1 corresponds to $A_V \approx 6.0 \pm 0.7$. This sets an upper limit because the source is only $\sim$1.5 kpc away. Moreover, the method of Schlegel et al. (1998) is known to overestimate the extinction for dense regions by a factor of 1.3–1.5 (e.g., Arce & Goodman 1999). Thus, it is likely that $A_V \sim 3–4$, consistent with the earlier estimates by van Dishoeck et al. (1993).

There is another bright pointlike source, 2MASS J06180359+2227227 (=HST N8JT007783), projected onto the area of source 1. The source is clearly seen in the optical and near-IR bands ($B = 16.3 \pm 0.4$, $V = 14.5 \pm 0.3$, $J = 12.50 \pm 0.03$, $H = 11.88 \pm 0.03$, $K_s = 11.73 \pm 0.02$). The dereddened K_s flux of the source ranges from 20.1 to 27.6 mJy, that is, $(3.6–5.0) \times 10^{-12}$ ergs cm^{-2} s^{-1}. Most likely, 2MASS J06180359+2227227 is a foreground star.

An extended excess of IR emission is seen in the 24 μm mosaic map (Fig. 7, *left panel*), coinciding with the extended emission region detected with *Chandra* ACIS in the western part of source 1 and with 2MASS J06180378+2227314, an extended ($14'' \times 7''$) source of near-IR emission listed in the 2MASS XSC catalog with observed isophotal[11] $K_s = 12.86 \pm 0.12$. The excess is also seen in the 70 μm band (Fig. 7, *right panel*), its apparent size being comparable with the beam size. The aperture photometry estimates of the excess (with aperture corrections applied) are $11.4^{+1.9}_{-1.4}$ mJy (90% err.) $\pm$ 1.1 mJy (3 σ error of the pipeline) for the 24 μm band and 840^{+170}_{-480} mJy (90% err.) $\pm$ 170 mJy (3 σ error of the pipeline) for the 70 μm band. The apertures of a 6″and 8″radius were used for the 24 and 70 μm bands, respectively. These values correspond to $(2.8^{+0.48}_{-0.35} \pm 0.28) \times 10^{-13}$ ergs cm^{-2} s^{-1} for the 24 μm band and $(9.7^{+1.96}_{-5.52} \pm 1.96) \times 10^{-12}$ ergs cm^{-2} s^{-1} for the 70 μm band. Notice, that the latter value is actually an upper limit. Depending on the extinction value, the dereddened flux of 2MASS J06180378+2227314 is 6.4–10.7 mJy, that is $(1.2–1.9) \times 10^{-12}$ ergs cm^{-2} s^{-1} in the K_s band.

The extended source is seen neither in the J and H bands of the 2MASS survey (Skrutskie et al. 2006) nor in the archival blue, red, and infrared images of the POSS-II survey (Reid et al. 1991). With the `daophot` package (Stetson 1987) integrated into the NOAO IRAF software suite, the following upper limits were obtained for 2MASS J06180378+2227314: 6.6×10^{-13} ergs cm^{-2} s^{-1} in the 2MASS J band, 2.9×10^{-13} ergs cm^{-2} s^{-1} in the 2MASS H band, 8.0×10^{-11} ergs cm^{-2} s^{-1} in the POSS-II blue band (3750–5500 Å), 3.0×10^{-12} ergs cm^{-2} s^{-1} in the POSS-II red band (5900–7100 Å), and 3.0×10^{-11} ergs cm^{-2} s^{-1} in the POSS-II IR band (7350–8750 Å). The limits assume the estimated extinction for the source ($A_V = 6$).

The pointlike X-ray source source 3 is also seen as a weak IR source in all the bands of the 2MASS survey, with $J = 17.3 \pm 0.3$, $H = 16.8 \pm 0.6$, $K_s = 16.2 \pm 0.4$ (see Fig. 8, *bottom panels*).

4. DISCUSSION

Below we discuss the multiwavelength data obtained for the $\sim$1.5′ region that includes source 1 and source 3 and some implications of the data analysis. We will refer to this extended source as J0618.

The results of the multiwavelength data analysis presented above can be summarized as follows. The hard extended X-ray source source 1 consists of "clumps," both extended (source 1a) and pointlike (source 1b), which emit hard X-ray continuum. There are signatures of a thermal component of temperature $\sim$0.2 keV in the spectrum of source 1a, and of X-ray line emitting clumps side by side with an extended IR source. The X-ray morphology of the extended source J0618 is complex. source 3 is pointlike according to the *Chandra* observations. The *XMM-Newton* image in Figure 2 shows evidence for an extended bridge of diffuse emission connecting source 1 with source 3. Longer observations are needed to establish firmly the possible presence of this faint bridge and of an X-ray halo around source 3 (see, e.g., Fig. 6).

The X-ray spectra of sources 1a and 1b and source 3 are characterized by power-law components with photon indices $\Gamma \sim 1.5$. The spectrum of the source 1 region shows a feature at about 1.8 keV with a flux of a few times 10^{-7} photons cm^{-2} s^{-1} at the 90% confidence level, which might be attributed to a Si K-shell line. A feature at 3.7 keV was found in the X-ray spectrum of source 3 at the 99% confidence level, which might be attributed to an Ar K-shell line, unless the line is a redshifted Fe K line of an extragalactic source. A firm detection of the lines from the localized clumps with *XMM-Newton* is hampered by the presence of strong hard nonthermal continuum emission.

[11] See http://www.ipac.caltech.edu/2mass/releases/allsky/doc/sec4_5e.html.

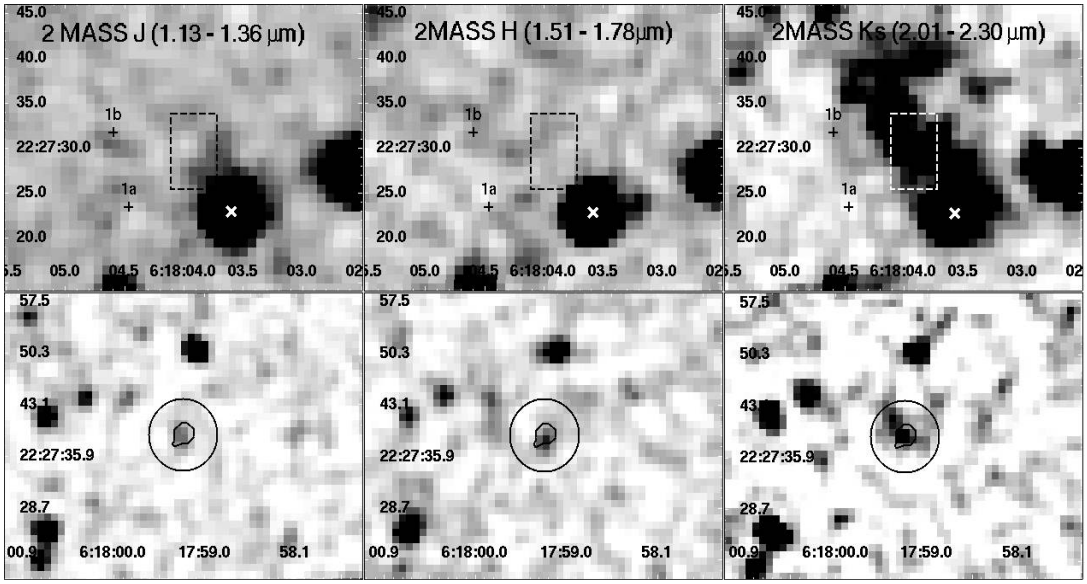

FIG. 8.— *Top panels*: Source 1 environment in the 2MASS near-IR bands. The source regions and positions are marked in the same manner as in Fig. 7. The white X-mark denotes the position of 2MASS J06180359+2227227. *Bottom panels*: Surroundings of source 3 in the 2MASS near-IR bands. The 10″ radius circle denotes the region used for spectral analysis of the X-ray data. The contour inside the circle denotes the position of source 3 as seen by *Chandra* in the 0.3–10 keV band at the 2.5×10^{-5} counts s^{-1} $pixel^{-1}$ level.

An extended source of IR emission was found at the northwestern edge of source 1 with a dereddened flux in the 24 μm band of *Spitzer* MIPS of about 3×10^{-13} ergs cm^{-2} s^{-1} and an upper limit for the 70 μm band of about 10^{-11} ergs cm^{-2} s^{-1}. The near-IR flux of the source is about 2×10^{-12} ergs cm^{-2} s^{-1} in the 2MASS K_s band. The source is not seen in the J and H bands of the 2MASS survey, nor in the POSS-II optical bands. The upper limits are 3×10^{-13} ergs cm^{-2} s^{-1} for the H band, 7×10^{-13} ergs cm^{-2} s^{-1} for the J band, 3×10^{-11} ergs cm^{-2} s^{-1} for the POSS-II infrared band (0.7–0.9 μm), 3×10^{-12} ergs cm^{-2} s^{-1} for the POSS-II red band (0.6–0.7 μm), and 8×10^{-11} ergs cm^{-2} s^{-1} for the POSS-II blue band (0.4–0.6 μm). These upper limits are used below to constrain the model we propose for J0618.

Earlier studies of molecular emission from the extended region of apparent interaction of the IC 443 SNR with the neighboring molecular cloud have indicated the presence of emission from both fast and slow shocks (e.g., Burton et al. 1988; Dickman et al. 1992; van Dishoeck et al. 1993, Snell et al. 2005). Molecular clouds are known to have highly inhomogeneous internal structure (e.g., Blitz 1993). A molecular cloud consists of numerous dense clumps with a rather small volume filling factor, embedded in an interclump matter of a modest density of 5–20 cm^{-3}. The presence of a wide range of dense molecular emission clumps down to about 1″scale has been established in the cloud around source 1 by Richter et al. (1995).

The apparent coincidence of the extended structured nonthermal X-ray continuum source J0618 with local excesses of IR emission can be understood in the framework of a model of interaction of a molecular cloud with a fast ballistically moving object. If the object was ejected by a SNR, it could be either a massive fast-moving ejecta knot or a pulsar wind nebula. In both cases shock waves will be driven into the cold matter of the cloud. Such a scenario and the expected properties of the emitted IR and X-ray radiation will be discussed below. A large power (above 10^{35} ergs s^{-1}) released by a fragment of velocity about 300 km s^{-1} being decelerated by a dense cloud is emitted as UV photons. The UV emission will create an H II region surrounding the fragment. The detected *Spitzer* emission and all of the IR/optical upper limits are consistent with the continuum emission of an H II region of a temperature about 10^4 K and a number density above 100 cm^{-3}. However, to explain the detected near-IR flux of the source in the 2MASS K_s band one should consider an additional emission component most likely due to line emission of shocked molecular hydrogen. The radio, IR, and optical emission of the H II region surrounding J0618 will be addressed in §§ 4.2 and 4.3.

4.1. *X-Ray Emission from Isolated Fast Ejecta Fragments*

An important distinctive feature of J0618 is the presence of extended nonthermal hard X-ray emission. This can be explained in the framework of a model of interaction of a massive isolated ejecta fragment moving with a velocity above 300 km s^{-1} through a molecular cloud. In the model by Bykov (2002, 2003), X-ray emission from an ejecta fragment of 0.2–0.3 pc size (∼30″–40″ at 1.5 kpc, the angular size of such a fragment in IC 443), interacting with a molecular cloud was estimated. The fragment mass was assumed to be $\gtrsim 10^{-2}\,M_\odot$, containing $\sim 10^{-4}\,M_\odot$ of Si. The "knot" traveled through an interclump medium of a number density ∼100 cm^{-3} with a velocity of ∼500 km s^{-1} (the corresponding postshock temperature is ∼0.3 keV). The model predicts a hard continuum emission with a photon index $\Gamma \lesssim 1.5$ and 1.8 keV Si line emission with a flux of $\sim 10^{-6}$ photons cm^{-2} s^{-1}. The K-shell lines are excited by both nonthermal and thermal electrons.

In the case of J0618, a slightly more massive fragment highly structured due to interaction with the dense molecular clump would be more realistic. A range of subfragment velocities around the mean value ∼200–300 km s^{-1} is consistent with the age of IC 443 of about 30,000 yr advocated by Chevalier (1999). Such a fragment would provide line fluxes of a few times 10^{-7} photons cm^{-2} s^{-1}, consistent with the estimated fluxes of the putative Si and Ar lines (Fig. 4) from J0618. The effects of clumping of the metal-rich ejecta would result in an intermittent spatial structure of X-ray line emission from the source. It is worth to mention that the intrinsic absorbing column $\Delta N_{\rm H}$ of a fragment could be substantial ($>10^{21}$ cm^{-2}), especially if the fragment contains metal-rich ejecta material.

The relatively low velocity and the high absorbing column of an ejecta fragment in a dense molecular cloud makes its observational appearance to be very different from that observed in Vela shrapnel A. The observed emission of Vela shrapnel A is strongly dominated by an optically thin thermal component (of T about 0.5 keV) of a shock heated plasma (Miyata et al. 2001). Contrary to the Vela case, a thermal emission of a thin plasma of temperature $\sim$0.1 keV is not the main component in the observed X-ray spectra of J0618 because of the high absorption. A hard nonthermal emission dominates the X-ray spectrum of J0618.

4.2. *Energetics of an X-Ray-Emitting SN Ejecta Fragment*

The models of an isolated X-ray source involving the interaction of a supernova blast wave with dense ambient matter suggest that the keV emission is due to bremsstrahlung of shock-accelerated electrons (Bykov et al. 2000; Bykov 2002). Synchrotron X-ray emission would require electrons with TeV energies accelerated by shocks of speed well above 1000 km s^{-1}, which is hard to expect for a middle-aged SNR in a dense ambient medium, unless the moving object is a pulsar wind nebula.

The radiative efficiency of nonthermal bremsstrahlung is known to be low at keV energies. This means that to producee a hard X-ray continuum at a rate $\dot{\epsilon}_r$, an electron of energy E_e dissipates energy at a rate $\dot{\epsilon}_e$ via Coulomb losses in a medium of an average charge Z, and $\dot{\epsilon}_r/\dot{\epsilon}_e \approx 6.3\times10^{-4}Z(E_e/m_ec^2)$—see, e.g., Akhiezer & Berestetsky (1957). Therefore, to produce the X-ray emission at the observed level of about $6\times10^{31}d_{1.5}^2$ ergs s^{-1} by electrons accelerated to 50–100 keV, the dissipated power must be about $\dot{\epsilon}_e \approx 10^{35}d_{1.5}^2Z^{-1}(m_ec^2/E_e)$ ergs s^{-1}. The total dissipated power $\dot{\epsilon}_{\rm kin} = 10\dot{\epsilon}_e\eta_{-1}^{-1}$. Here $\eta_{-1} \equiv \eta/0.1 \lesssim 1$ is the efficiency of electron acceleration by a shock, providing $\dot{\epsilon}_{\rm kin} \sim 10^{37}d_{1.5}^2Z^{-1}\times\eta_{-1}^{-1}$ ergs s^{-1}.The electron energy $E_e = 50$ keV was assumed in the estimation. Since $Z \lesssim 10$ in an oxygen/silicon-rich gas an enhanced metallicity of an ejecta fragment (dependent on mixing of the ejecta with the ambient matter) could somewhat compensate the bremsstrahlung inefficiency providing $\dot{\epsilon}_{\rm kin} \sim 10^{36}d_{1.5}^2$ ergs s^{-1}. Note that the power required to produce radio-emitting relativistic electrons in clump D is also just above $10^{36}d_{1.5}^2$ ergs s^{-1}.

The upstream ram pressure power dissipated at the forward shock of a ballistically moving fragment, $\dot{\epsilon}_{\rm sh} \approx 8\times10^{35}n_{a3}v_2^3r_{20}^2d_{1.5}^2$, is the source of gas heating and particle acceleration. Here r_{20} is the shock radius of J0618 (measured in 20″). The mechanical power $\dot{\epsilon}_{\rm kin}$ in the shock model must not exceed $\dot{\epsilon}_{\rm sh}$, resulting in the condition $n_{a3}v_2^3r_{20}^2Z\eta_{-1} \geq 12$ to be fulfilled. Therefore, ejecta fragments of velocity $v_2 \sim 2$ moving through a cloud of density $n_{a3} \sim 0.2$ will have $\dot{\epsilon}_{\rm sh} \approx \dot{\epsilon}_{\rm kin}$, if $Z \gtrsim 2$. Thus, the observed patchy structure of the X-ray emission that is apparent in the *Chandra* ACIS images of J0618 could be attributed to structured metal clumps of the ejecta of IC 443.

How can one directly detect or constrain the power dissipated by the shock in the model of IC 443 ejecta fragment ballistically moving through a molecular cloud? The gas temperature behind the standard single-fluid strong MHD shock can be estimated as $T \approx 1.4\times10^5v_2^2$ (K). For a shock with energetic particle acceleration efficiency $\gtrsim$10% that we consider here the postshock temperature should be reduced by a factor of about 1.2 to account for the effects of the energy flux carried away with energetic particles (see, e.g., Bykov 2002). The postshock gas cooling distance estimated by Hartigan et al. (1987) is about $1.8\times10^{13}v_2^{4.67}n_{a3}^{-1}$ cm. The shock of a velocity 300 km s^{-1} in the molecular cloud is radiative with the cooling layer angular size of $0.15''n_{a3}^{-1}$. If the extended structure of source 1a seen in Figure 2 of BBP05 is indeed due to the thermal emission of hot postshock gas then $n_{a3} \sim 0.03$ would explain both the extension of about 5″and the luminosity of soft thermal component below 10^{32} ergs s^{-1} discussed in BBP05. Most of the shock power, however, is not in the soft X-ray emission of shock-heated gas, but rather in UV–optical emission of the radiative shock dominated by UV lines of O VI at 1035 Å, Lyα and He II at 304 Å (e.g., Hartigan et al. 1987).

At the same time the UV photons produced by the radiative bow shock of ejecta fragment with a luminosity $L_{\rm UV} = 10^{36}$ ergs s^{-1} L_{36}, will be absorbed and reprocessed, mostly to IR emission, in an expanding H II region surrounding the bow shock of J0618. Note here that the shape of the H II region could be different from that of the nonthermal X-ray nebulae, but it should overrun the bow shock of J0618. From the apparent position of J0618 in the molecular cloud and the estimated fragment velocity one may conclude that it entered the molecular cloud about 1000 yr ago. Assuming that all of the UV photons produced by the radiative bow shock are absorbed in a spherical layer of an homogeneous ambient matter, one can obtain the estimation of the H II region radius of about $6\times10^{17}L_{36}^{1/3}n_{a3}^{-2/3}$ cm (see, e.g., Spitzer 1978). In fact, the geometry of J0618 is more complex than a spherical H II region because of the motion of the extended emitting fragment and because of the strong inhomogeneity of the ambient molecular cloud down to the arcsecond scale as was observed by Richter et al. (1995). In the interclump matter of density below 100 cm^{-3} the scale size of the H II region would exceed the apparent X-ray size of J0618. On the other hand, the number density of the clump D located in a close vicinity of J0618 was estimated by van Dishoeck et al. (1993) to be above 10^3 cm^{-3} and the size of the H II region is consistent with the size of the 24 μm emission excess around clump D [of about $(2–3)\times10^{-11}$ ergs cm^{-2} s^{-1}] apparent in *Spitzer* image presented in the right panel of Figure 6. Although very simplified, such a model allows us to estimate the radio, IR, and optical emission of the shock-produced H II region.

4.3. *Radio–IR–Optical Continuum and Line Emission of the* H II *Region*

The emission of the H II region consists both of continuum emission of a thin thermal plasma of a kinetic temperature about 10,000 K and of a rich emission-line spectrum (see, e.g., Spitzer 1978). The specific appearance and the chemistry of the mostly neutral photodissociation region in molecular clouds were reviewed by Hollenbach & Tielens (1999). In the standard case the interstellar H II regions are powered by massive luminous stars. In the case of J0618 the source of the ionizing radiation is an extended fast-moving bow shock and the ionized region is likely unsteady. That makes an accurate modeling of the system rather complicated, so we shall present here some approximate estimations of the expected IR/optical fluxes from the H II region. The observed 24 μm *Spitzer* MIPS, 2MASS K_s, and 1.4 GHz radio emission, as well as the upper limits provided by the other *Spitzer*, 2MASS and POSS-II observations of J0618 were modeled as continuum emission of a hot ionized plasma of a temperature ranging from 8000 to 20,000 K. The modeled fluxes were corrected for interstellar extinction for a wide range of A_V values below 8, since $A_V \sim 8$ roughly corresponds to $N_{\rm H} \sim 1.5\times10^{22}$ cm^{-2}—the maximal value allowed by the fits to the *Chandra* data presented in Figure 3. Thus all the optical and IR measurements of J0618 were used to constrain both the kinetic temperature of the H II region and the parameter $Y = n_{e3}^2r_{20}^3$, where n_{e3} is the electron number density in the H II region measured in units of 10^3 cm^{-3}, and r_{20} is defined in § 4.2. It was found that the measured 24 μm flux of the source can be explained by a thermal continuum of a 10,000 K temperature H II region and $Y \sim 0.03$ with $A_V \gtrsim 6$. Since the continuum emissivity is $\propto n_{e3}^2$ the apparent

patchy image of 24 μm emission could be due to the clumpy structure of the ejecta fragment.

The continuum emission from the H II region is consistent with the upper limits obtained from *Spitzer*, 2MASS, and POSS-II observations of J0618. The radio flux density from such an H II region is about 30 mJy. The flux density obtained by integrating the 1.4 GHz radio emission over a larger (an arcminute scale size) region with VLA was about 60 mJy. Therefore, the 1.4 GHz radio flux is not in a conflict with the H II region model for the parameter $Y \sim 0.03$. We found also that the flux of the hydrogen recombination Hα line from the H II region is below the upper limit of 3×10^{-12} ergs cm^{-2} s^{-1} obtained from the POSS-II red band (0.6–0.7 μm) observation discussed above.

The estimated parameter $Y \sim 0.03$ corresponds roughly to $n_e \sim 160$ cm^{-3}. The bow-shock radius estimated from X-ray image is $r_{20} \sim 1$ implying that the derived electron density in the bright part of the H II region in J0618 is dominated by the compressed postshock flow. Then the preshock ambient density in the radiative shock can be estimated from $n_a < n_e/4$, providing the ambient gas density $\lesssim$40 cm^{-3}, generally consistent with that expected in the interclump matter of a molecular cloud. A substantial part of the powerful UV emission from the radiative shock of J0618 will irradiate the nearby dense molecular clump D, providing another H II region of a surface brightness and high luminosity well in excess of that from J0618 that is clearly seen in Figure 6. In the frame of the ejecta fragment model of J0618 we estimated that at least a substantial amount of 24 μm flux from clump D [that is about $(2–3) \times 10^{-11}$ ergs cm^{-2}s^{-1}] can be attributed to the H II region excited by the UV emission from the nearby source J0618.

That model provides, however, only about one-third of the observed 2MASS K_s-band flux of J0618, and that cannot be simply relaxed with an appropriate H II region parameters choice. Thus, an extra contribution in the 2MASS K_s band at the level of $\sim 1.5 \times 10^{-12}$ ergs cm^{-2} s^{-1} is required. That contribution may come, most likely, from the emission lines of the shocked molecular hydrogen in J0618 and would require the presence of C-type molecular shocks of velocity $\sim$30 km s^{-1} in the close vicinity of J0618. Moreover, the atomic fine-structure lines could contribute to the 24 μm emission detected by *Spitzer* MIPS if supernova ejecta drive J-type shocks of about 100 km s^{-1} (and faster) into dense molecular clumps. We discussed above only the emission produced by the forward bow shock of the fragment; however; slower reverse shock will also be present and since the ejecta fragment body is likely very inhomogeneous the real structure is likely even more complex. Relevant line emission models are briefly reviewed in the next subsection.

4.4. *IR Line Emission in Radiative Shock Models*

Atomic fine-structure lines of [O I] (63 μm) and [Fe II] (26 μm) could dominate the emission in the *Spitzer* MIPS 70 and 24 μm bands. The lines are known to trace fast radiative shocks in molecular cloud material. A comprehensive study of radiative shocks in interstellar clouds has been done by Hollenbach & McKee (1989, hereafter HM89). They have shown that the intensity ratio of [O I](63 μm)/[Fe II](26 μm) is about 10 for a shock wave in a cloud of a density $n_{\rm cl} = 10^3$ cm^{-3}. They estimated the [O I] (63 μm) IR line intensity as $I_{63} \approx 1.5 \times 10^{-3}$ ergs s^{-1} sr^{-1} for a shock of a velocity $v_{\rm sh} = 150$ km s^{-1} and demonstrated that it scales roughly linearly with $n_{\rm cl} v_{\rm sh}$. The combination of optical line emission of O I at 6300 Å, C II (2326 Å), and O II (3726 Å) provides the dominating gas coolant in transparent systems of $n_{\rm cl} \leq 10^4$ cm^{-3}. The line intensities were obtained by HM89 under the assumption of standard solar composition with account for the interstellar gas depletion to dust grains. The IR-optical line intensities from shocks driven by (and into) metal-rich ejecta could be produced with lower preshock number densities $n_{\rm cl}$ than those modeled by HM89, and should be rescaled, respectively. This can reduce the preshock density required to match the observed fluxes.

Applying the HM89 model intensities to an IR source of an angular area A_{100} (measured in units of 100 arcsec^2) as discussed in § 3.2, one obtains a [Fe II] (26 μm) line flux $F_{26} \approx 2.4 \times 10^{-13} A_{100} n_3 v_2$ ergs cm^{-2} s^{-1}. Here n_3 is the preshock number density in units of 10^3 cm^{-3} and v_2 is the shock velocity in 10^2 km s^{-1}. To reach the 24 μm flux of about 3×10^{-13} ergs cm^{-2} s^{-1} as estimated from the *Spitzer* MIPS data, one would need $n_3 v_2 A_{100} \sim 1$. As the estimated emission area is $A_{100} \sim 2$, one needs $n_3 v_2 \sim 0.5$ to account for the observed IR emission. The [Fe II](26 μm) line could provide a sizeable part of the 24 μm *Spitzer* MIPS flux. The associated model flux of the [O I] (63 μm) line, $F_{63} \approx 2.4 \times 10^{-12}\ A_{100} n_3 v_2$ ergs cm^{-2} s^{-1} is consistent with the upper limit derived above. It is apparent from Figure 2 that source 1 is located near the shocked molecular clump D presented in a map by van Dishoeck et al. (1993). Typical densities of molecular clumps, studied by van Dishoeck et al. (1993) are $\gtrsim 10^4$ cm^{-3}. The condition $n_3 v_2 \sim 0.5$ can be matched by either a slow shock of velocity $v_2 \sim 0.3$ in the outskirts of clump D, or by a fast shock of $v_2 \sim 1$ in the interclump medium.

Near-IR metastable lines of Fe II at 1.3 and 1.7 μm have a rather flat shock velocity dependence above 100 km s^{-1}. The intensity of the brighter Fe II line at 1.3 μm scales roughly linearly with $n_{\rm cl}$, and it is about $0.2 I_{63}$. This estimate is close to, but still consistent with the upper limit of the flux in the 2MASS J band discussed in § 3.2. A near-IR NI (1.04 μm) line flux was predicted by HM89 to be at the level comparable with that of [O I] (63 μm), and a S I (1.1 μm) line flux similar to that of Fe II at 1.3 μm.

From the apparent lack of extended emission in the POSS-II red band (0.6–0.7 μm) the flux upper limit for O I (6300 Å) can be estimated as 3×10^{-12} ergs cm^{-2} s^{-1} (assuming the reasonable extinction to source 1 as $A_V \approx 6$). The flux limit is below the value predicted by HM89 for the O I(6300 Å)/[Fe II](26 μm) ratio for a transparent system with shock velocity $v_2 \gtrsim 1$. However, the line ratio is increasing with shock velocity for $v_2 < 1$, and, for example, a fast J-type (see Draine 1980 for a definition of J- and C-type shocks) radiative shock of $v_2 \sim 0.6$ in a medium of $n_3 \sim 1$, could explain both the observed [Fe II] 26 μm line flux and the derived upper limit for the O I (6300 Å) line flux. Note that optical line fluxes from a radiative shock propagating into oxygen-rich ejecta material could be reduced by heat-conduction effects (e.g., Borkowski & Shull 1990).

An important diagnostic IR-line ratio sensitive to the shock velocity is [Ne II](12.8 μm)/[Fe II](26 μm). The ESO VLT Spectrometer and Imager for the Mid-Infrared (VISIR) is an optimal instrument for observations in the two mid-infrared atmospheric windows: the 8–13 μm N band with a $19.2'' \times 19.2''$ FOV and the 16.5–24.5 μm Q band with a $32.3'' \times 32.3''$ FOV (Lagage et al. 2006). The spectrometer could detect [Ne II](12.8 μm) predicted by the radiative shock model of HM89 and the continuum emission from source 1 H II region, thus discriminating between the two models.

The model of a single fast radiative J-type shock developed by HM89 underpredicts the near-IR flux (above 10^{-12} ergs cm^{-2} s^{-1}) observed in the K_s band from the extended source 2MASS J06180378+2227314, closely associated with the *Spitzer* MIPS 24 μm excess (Fig. 7). Thus, a combination of fast and slow shocks is needed to explain the IR emission from J0618. The same conclusion has been made in most of the studies of molecular

emission of the southwestern region of IC 443. Burton et al. (1990) argued that both fast dissociative J-type and slow C-type shocks must be present in the extended southern cloud of IC 443 to explain the observed line fluxes (see also Snell et al. 2005 for a recent discussion). Analyzing different shock models, including a time-dependent one, Snell et al. (2005) concluded that no single-shock model can explain the existing observations, and a range of shock velocities is required.

4.5. *Shocks in a Molecular Cloud Driven by Ejecta Fragments*

A wide range of shock velocities in a molecular cloud is required to explain the IR and X-ray observations of source 1. Slow molecular C-type shocks are required to explain the observed 2MASS K_s band emission.

Molecular emission occurs when a fast ejecta fragment collides with molecular clumps of different densities, $\rho_{\rm cl}$, producing multiple shocks of velocities $v_s \propto \rho_{\rm cl}^{-1/2}$. This can explain the shock velocity range of 10 km s^{-1} $\leq v_{\rm s} \leq$ 100 km s^{-1}, required to explain both the fluxes detected by *Spitzer* MIPS and 2MASS K_s and the upper limits on the optical lines.

In the considered case the presence of a fast shock of velocity $\gtrsim$300 km s^{-1} seems to be required to explain the X-ray data discussed above. Moreover, it is apparent from Figure 1 that while the 1.4 GHz radio emission is dim in the southeastern part of the shocked molecular cloud in comparison with that at the northeast, there is a localized excess in the vicinity of molecular clump D adjacent to J0618. If the radio emission is the synchrotron emission produced by relativistic electrons in the GeV regime in a likely enhanced magnetic field of the dense clump D, then the model requires the presence of a fast shock of velocity well above 100 km s^{-1} to accelerate the relativistic particles in the vicinity of source 1.

The shock ram pressure estimations for multiple shock models were discussed by many authors (e.g., Burton et al. 1990; Richter et al. 1995; Cesarsky et al. 1999; Snell et al. 2005). A fast shock of velocity $v_{\rm s} \sim 50$–100 km s^{-1} incident on a clump of a moderate number density 10^3–10^4 cm^{-3} would have a high ram pressure $nv^2 \sim 10^7$ 10^8 cm^{-3} (km s^{-1})^2. It seems to be uneasy to attribute the estimated range of ram pressures to a uniform SN blast wave colliding with a cloud. A SN blast-wave ram pressure, as estimated from the properties of shocked X-ray-emitting gas inside the remnant, is smaller. On the other hand, strong ram-pressure inhomogeneities can be produced if a molecular cloud is hit by SN ejecta driving the blast wave. The ejecta are likely to be rather fragmented. Each can be considered as an ensemble of ejecta fragments with a range of velocities and densities produced by early ejecta instabilities. The fragments could provide a wide range of ram pressures in the molecular cloud (up to 10^8 cm^{-3} [km s^{-1}]^2) driving shocks of different velocities, which are required to explain the observational data. Isolated fast-moving dense ejecta fragments could penetrate deeper into the dense parts of the cloud driving the high-pressure shocks on relatively small scales.

4.6. *Time Variability and Ejecta Fragments Statistics*

The lifetime of an isolated ejecta fragment in a dense medium is an important factor with regard to time variability of the X-ray emission. A fast-moving knot is decelerating due to the interaction with the ambient gas. The drag deceleration time of a fragment of velocity v, mass $\mathcal{M}$, and radius $\mathcal{R}$ can be estimated as $\tau_d \approx 100 \mathcal{M}_{-2} (n_{a3} v_2 \mathcal{R}_{-1}^2)^{-1}$ yr. Here $\mathcal{R}_{-1} = \mathcal{R}/(0.1$ pc) and $\mathcal{M}_{-2} = \mathcal{M}/10^{-2}\ M_\odot$. The number density n_{a3} of the ambient matter is in units of 10^3 cm^{-3}, and the fragment velocity v_2 in units of 10^2 km s^{-1}. Hydrodynamical crushing of a fast knot occurs on a timescale $\tau_c \sim \chi^{1/2} \mathcal{R} v^{-1}$ (e.g., Chevalier 1975; Sutherland & Dopita 1995; Wang & Chevalier 2001 and references therein). The density contrast $\chi = \rho_k/\rho_a$ (ρ_k is the knot density) is of the order of 1 for a large enough fragment, and $\tau_d < \tau_c$ for large enough clumps. To reach its apparent position in the molecular cloud of IC 443, an isolated ejecta fragment must be massive enough, $\mathcal{M}_{-2} \gtrsim 1$, to overcome strong drag deceleration in the dense matter, as discussed below.

Particle acceleration occurs on a few-years timescale if the fast particle diffusion coefficient does not exceed 10^{22} cm^2 s^{-1} (see Bykov 2002 for a discussion). Thus, given the fragment lifetime estimated above, some time variability of the X-ray emission, both in hard continuum and lines, can be expected on a few-years timescale (and longer) for a fragment of velocity $v_2 \gtrsim 3$ in a dense ambient matter with $n_{a3} \gtrsim 3$, typical for molecular clumps. Variable X-ray emission has been recently observed with *Chandra* in a few molecular clouds in the Galactic center region by Muno et al. (2007). Using the above estimates, one can argue that variable X-ray emission could be produced due to an interaction of metal-rich supernova ejecta with dense clumps of molecular clouds.

According to the $\log N - \log S$ distribution of X-ray-emitting knots simulated by the method of Bykov (2003), the probability of another similarly bright ejecta fragment getting into the field is rather low because of the short lifetime of the fragment in a dense molecular clump. However, some smaller and less massive fragments propagating in the interclump medium could be seen in the cloud as weak pointlike X-ray sources of luminosities $L_{\rm X} \lesssim 10^{31}$ ergs s^{-1}. In order to firmly identify the sources as such fragments, a deeper observation is required.

The hydrodynamic simulations available (Klein et al. 1994; Wang & Chevalier 2001) predict a complex irregular structure of the fragment body due to hydrodynamic instabilities. In this case the X-ray image would show an irregular patchy structure, instead of a smooth regular head-tail structure. The patches are due to emission of dense pieces of the fragmented knot illuminated by the shock-accelerated energetic particles. The observed morphology of X-ray emission with bright clumps of a few arcseconds size in source 1, such as source 1a and source 1b, as well as source 3, can be explained in that model. It is worth to note that ballistically moving ejecta fragments could have rather large nonradial velocities (with respect to the apparent center of SN explosion). The nonradial velocity components will be substantial if the fragments originate from ejecta instabilities at relatively late evolution stages.

Thus, one can conclude that the morphology, spectra, and X-ray luminosity of the J0618 complex are generally consistent with those expected for a ballistically moving SN ejecta fragment interacting with a molecular cloud, although it is worth to discuss also some alternatives.

4.7. *Alternative Interpretations of J0618*

A possible interpretation of the extended hard X-ray source J0618 associating it with an interaction of the ejecta of SNR IC 443 with the nearby molecular cloud has been discussed above in some detail. Another SNR-related possible interpretation is a low-luminosity pulsar wind nebula originating either from IC 443 or from another SNR G189.6+3.3, advanced by BBP05.

Extragalactic sources could also contribute to the observed appearance of J0618. Spectra the of pointlike sources source 2 and source 3 could be interpreted as that of AGNs. Within such an interpretation the feature at about 3.7 keV in the spectrum of source 3 could correspond to a redshifted (with $0.6 < z < 1$) Fe emission line. Moreover, one could speculate on the association of the extended source 1 with a high-z cluster of galaxies. The

angular size of source 1 ($< 1'$at photon energies >2 keV) would suggest in that case a redshift $z > 0.5$ (see, e.g., Rosati 2004 for a review of high-z clusters). The thermal fit of the diffuse source 1^* presented in Table 3 with the temperature about 5 keV is consistent with the cluster interpretation.

Optical and IR identifications of galaxies (of a few arcsecond scale size at $z \sim 1$) in the hypothetical cluster are the most obvious test to check the interpretation and measure the redshift of the putative cluster. With the optical data available and given the substantial absorption ($3 < A_V < 6$), it is possible to identify the objects not fainter than $m_V = 17$–19, while the brightest galaxies in most of the known X-ray clusters at $z \lesssim 1$ are of $m_V \gtrsim 19$–20. Thus a dedicated optical-IR study is needed to confirm or reject the high-z galaxy cluster interpretation. The observed extension of the 2MASS K_s source correlated with observed diffuse X-ray emission is not easy to understand in the cluster of galaxies interpretation; it rather supports a Galactic SNR-related origin of J0618.

5. CONCLUSIONS

The multiwavelength observations presented here indicate a possible physical connection of the X-ray source J0618 with the neighboring IR *Spitzer* and 2MASS sources. That connection, if real, can be understood in a scenario where J0618 originates in an interaction of the IC 443 SNR with the adjacent molecular cloud. The correlation would require the presence of both fast and slow shocks in the clumpy molecular-cloud material. The X-ray line features apparent in the spectra of the clumps favor a scenario in which the shocks are produced by a fast ballistically moving SN ejecta fragment penetrating into a structured molecular cloud. The model provides a physical picture coherent with the current observational data, although alternative scenario cannot be rejected yet.

Alternatively, source 1 can be interpreted as a massive X-ray cluster of galaxies at a redshift $z > 0.5$. High-resolution arcsecond-scale observations and fine spectroscopy are required to distinguish between these very different scenarios.

If the SNR-ejecta interpretation is confirmed by further observations, the source J0618 in the IC 443 could be a prototype of a rather numerous population of hard X-ray–IR sources created by SN explosions in the dense environments of star-forming regions. Such sources would be particularly abundant in the Galactic center region.

We thank the anonymous referee for careful reading of our paper and useful comments. This investigation is based on observations obtained with *Chandra*, which is operated by the Smithsonian Astrophysical Observatory on behalf of NASA, and *XMM-Newton*, an ESA science mission with instruments and contributions directly funded by ESA Member States and NASA. This work is based in part on observations made with the *Spitzer Space Telescope*, which is operated by the Jet Propulsion Laboratory, California Institute of Technology under a contract with NASA. This research has made use of data obtained from the High Energy Astrophysics Science Archive Research Center (HEASARC), provided by NASA's Goddard Space Flight Center. This research has made use of SAOImage DS9, developed by Smithsonian Astrophysical Observatory. Some of the calculations were performed at the Supercomputing Centre (SCC) of the A. F. Ioffe Institute, St. Petersburg. A. M. B. and F. B. thank ISSI (Bern) for a stimulating team meeting on SNRs.

Support for this work was partly provided by NASA through grants NNX06AE53G and NAG5-10865 and by RBRF grant 06-02-16844, by the Russian Leading Scientific Schools grant NSh-9879.2006.2, by the "Extended Objects in the Universe" program of OFN RAS, and by the "Origin and Evolution of Stars and Galaxies" program of RAS Presidium. F. B. acknowledges financial contribution from contract ASI-INAF I/023/05/0. A. M. K. thanks Yu. A. Shibanov for a valuable discussion on reduction of optical and IR images.

REFERENCES

Akhiezer, A. I., & Berestetsky, V. B. 1957, Quantum Electrodynamics (transl. Consultants Bureau, Inc.; Oak Ridge: Tech. Information Service Ext.)
Albert, J., et al. 2007, ApJ, 664, L87
Arce, H. G., & Goodman, A. A. 1999, ApJ, 512, L135
Asaoka, I., & Aschenbach, B. 1994, A&A, 284, 573
Aschenbach, B., Egger, R., & Trümper, J. 1995, Nature, 373, 587
Blair, W. P., et al. 2000, ApJ, 537, 667
Blitz, L. 1993, in Protostars and Planets III, ed. E. H. Levy & J. I. Lunine (Tucson: Univ. of Arizona), 125
Bocchino, F., & Bykov, A. M. 2000, A&A, 362, L29
———. 2001, A&A, 376, 248
———. 2003, A&A, 400, 203 (BB03)
Borkowski, K. J., & Shull, J. M. 1990, ApJ, 348, 169
Braun, R., & Strom, R. J. 1986, A&A, 164, 193
Burton, M. G. 1987, QJRAS, 28, 269
Burton, M. G., Geballe, T. R., Brand, P. W. J. L., & Webster, A. S. 1988, MNRAS, 231, 617
Burton, M. G., Hollenbach, D. J., Haas, M. R., & Erickson, E. F. 1990, ApJ, 355, 197
Bykov, A. M. 2002, A&A, 390, 327
———. 2003, A&A, 410, L5
Bykov, A. M., Bocchino, F., & Pavlov, G. G. 2005, ApJ, 624, L41 (BBP05)
Bykov, A. M., Chevalier, R. A., Ellison, D. C., & Uvarov, Yu.A. 2000, ApJ, 538, 203
Cesarsky, D., Cox, P., Pineau des Forets, G., van Dishoeck, E. F., Boulanger, F., & Wright, C. M. 1999, A&A, 348, 945
Chevalier, R. A. 1975, ApJ, 200, 698
———. 1999, ApJ, 511, 798
Chevalier, R. A., & Kirshner, R. P. 1979, ApJ, 233, 154
Claussen, M. J., Frail, D. A., Goss, W. M., & Gaume, R. A. 1997, ApJ, 489, 143
Cornett, R. H., Chin, G., & Knapp, G. R. 1977, A&A, 54, 889
DeNoyer, L. K. 1979, ApJ, 232, L165
Dickman, R. L., Snell, R. L., Ziurys, L. M., & Huang, Y.-L. 1992, ApJ, 400, 203
Draine, B. T. 1980, ApJ, 241, 1021
Esposito, J. A., Hunter, S. D., Kanbach, G., & Sreekumar, P. 1996, ApJ, 461, 820
Fesen, R. A., & Kirshner, R. P. 1980, ApJ, 242, 1023
Fesen, R. A., et al. 2006, ApJ, 645, 283
Johnson, R. P. 2006, in AIP Conf. Proc., 842, Particles and Nuclei, ed. P. D. Barnes (Melville: AIP), 1010
Gaensler, B. M., Chatterjee, S., Slane, P. O., van der Swaluw, E., Camilo, F., & Hughes, J. P. 2006, ApJ, 648, 1037
Green, D. A. 1986, MNRAS, 221, 473
Hartigan, P., Raymond, J., & Hartmann, L. 1987, ApJ, 316, 323
Hewitt, J. W., Yusef-Zadeh, F., Wardle, M., Roberts, D. A., & Kassim, N. E. 2006, ApJ, 652, 1288
Hollenbach, D., & McKee, C. F. 1989, ApJ, 342, 306
Hollenbach, D. J., & Tielens, A. G. G. M. 1999, Rev. Mod. Phys., 71, 173
Kaastra, J. S. 1992, An X-Ray Spectral Code for Optically Thin Plasmas (Int. SRON-Leiden Rep., updated ver. 2.0)
Kawasaki, M. T., Ozaki, M., Nagase, F., Masai, K., Ishida, M., & Petre, R. 2002, ApJ, 572, 897
Keohane, J. W., Petre, R., Gotthelf, E. V., Ozaki, M., & Koyama, K. 1997, ApJ, 484, 350
Klein, R. I., McKee, C. F., & Colella, P. 1994, ApJ, 420, 213
Lagage, P.-O., Pantin, E., Durand, G., Smette, A., Doucet, C., Belorgey, J., & Pel, J.-W. 2006, Proc. SPIE, 6269, 35
Leahy, D. A. 2004, AJ, 127, 2277
Makovoz, D., Roby, T., Khan, I., & Booth, H. 2006, Proc. SPIE, 6274, 10
Miyata, E., Tsunemi, H., Aschenbach, B., & Mori, K. 2001, ApJ, 559, L45
Morrison, R., McCammon, D. 1983, ApJ, 270, 119
Mufson, S. L., McCollough, M. L., Dickel, J. R., Petre, R., White, R., & Chevalier, R. 1986, AJ, 92, 1349

Muno, M., Baganoff, F. K., Brandt, W. N., Park, S., & Morris, M. R. 2007, ApJ, 656, L69
Olbert, C. M., Clearfield, C. R., Williams, N. E., Keohane, J. W., & Frail, D. A. 2001, ApJ, 554, L205
Petre, R., Szymkowiak, A. E., Seward, F. D., & Willingale, R. 1988, ApJ, 335, 215
Preite-Martinez, A., Feroci, M., Strom, R. G., & Mineo, T. 2000, in AIP Conf. Proc. 510, Fifth Compton Symposium, ed. M. L. McConnell & J. M. Ryan (Melville: AIP),73
Reich, W., Reich, P., & Fürst, E. 1990, A&AS, 83, 539
Reid, I. N., et al. 1991, PASP, 103, 661
Rho, J., Jarrett, T. H., Cutri, R. M., & Reach, W. T. 2001, ApJ, 547, 885
Richter, M. J., Graham, J. R., & Wright, G. S. 1995, ApJ, 454, 277
Rieke, G. H., et al. 2004, ApJS, 154, 25
Rosati, P. 2004, in Clusters of Galaxies, ed. J. S. Mulchaey A. Dressler, & A. Oemler (Cambridge: Cambridge Univ. Press), 72
Schlegel, D. J., Finkbeiner, D. P., & Davis, M. 1998, ApJ, 500, 525
Skrutskie, M. F., et al. 2006, AJ, 131, 1163
Snell, R. L., Hollenbach, D., Howe, J. E., Neufield, D. A., Kaufman, M. J., Melnick, G. J., Bergin, E. A., & Wang, Z. 2005, ApJ, 620, 758
Spitzer, L. 1978, Physical Processes in the Interstellar Medium (New York: Wiley)
Stetson, P. B. 1987, PASP, 99, 191
Sturner, S., Keohane, J., & Reimer, O. 2004, Adv. Space Res., 33, 429
Sutherland, R. S., & Dopita, M. A. 1995, ApJ, 439, 381
Tauber, J. A., Snell, R. L., Dickman, R. L., & Ziurys, L. M. 1994, ApJ, 421, 570
Troja, E., Bocchino, F., & Reale, F. 2006, ApJ, 649, 258
Turner, B. E., Chan, K.-W., Green, S., & Lubowich, D. A. 1992, ApJ, 399, 114
van Dishoeck, E. F., Jansen, D. J., & Phillips, T. G. 1993, A&A, 279, 541
Wang, C.-Y., & Chevalier, R. A. 2001, ApJ, 549, 1119
Wang, Z. R., Asaoka, I., Hayakawa, S., & Koyama, K. 1992, PASJ, 44, 303
Weisskopf, M. C., Karovska, M., Pavlov, G. G., Zavlin, V. E., & Clarke, T. 2007, Ap&SS, 308, 151
Werner, M. W., et al. 2004, ApJS, 154, 1
Winkler, P. F., & Long, K. S. 2006, AJ, 132, 360
Winkler, P. F., Kirshner, R. P. 1985, ApJ, 299, 981